Bioresource Technology 448 (2026) 134324

Contents lists available at ScienceDirect

Bioresource Technology

journal homepage: www.elsevier.com/locate/biortech

Unveiling the critical roles of iron and phosphorus in magnetic biochar derived from lithium-extraction residues of retired $LiFePO_4$ batteries for peroxymonosulfate activation toward ciprofloxacin degradation

Yue Fu [a], Yunqiang Yi [a,*], Weirui Chen [b], Yu Wang [a], Zenghui Diao [a], Jianying Qi [c]

[a] Key Laboratory of Green Processing and Intelligent Manufacturing of Lingnan Specialty Food, Ministry of Agriculture, College of Resources and Environment, Zhongkai University of Agriculture and Engineering, Guangzhou 510006, China
[b] Guangdong Key Laboratory of Environmental Catalysis and Health Risk Control, School of Environmental Science and Engineering, Institute of Environmental Healthand Pollution Control, Guangdong University of Technology, Guangzhou 510006, China
[c] College of Agriculture, South China Agricultural University, Guangzhou 510642, China

HIGHLIGHTS

- Magnetic biochar ($LFPBC_{0.5}$) was synthesized from recycled lithium-extraction residue.
- The degradation rate of ciprofloxacin in the $LFPBC_{0.5}$/PMS system reached 89.77%.
- Phosphorus doping promotes electron transfer and PMS adsorption in $LFPBC_{0.5}$.
- Radical and non-radical pathways co-drive the degradation of ciprofloxacin.

GRAPHICAL ABSTRACT

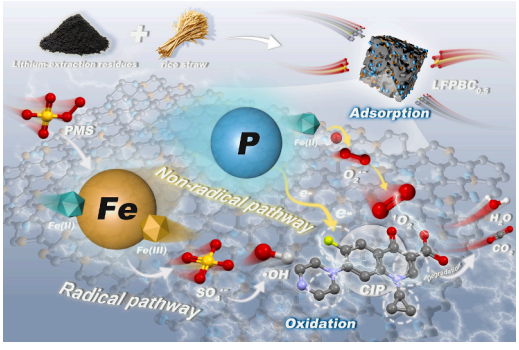

ARTICLE INFO

Keywords:
Magnetic biochar
Retired power batteries
Lithium-extracted residue
Advanced oxidation processes
Ciprofloxacin

ABSTRACT

The disposal of lithium-extraction residues from retired lithium iron phosphate ($LiFePO_4$) batteries and the removal of antibiotic contaminants from water are critical environmental concerns. Herein, a novel magnetic biochar ($LFPBC_{0.5}$) was synthesized using lithium-extraction residue and rice straw as raw materials to activate peroxymonosulfate (PMS) for efficient degradation of ciprofloxacin (CIP) in water. The $LFPBC_{0.5}$/PMS system achieved a CIP degradation efficiency of 89.77%, which was 1.60 and 2.33 times higher than that of the biochar (BC/PMS) and lithium-extraction residues (LFP/PMS) systems, respectively. The adsorption capacity of $LFPBC_{0.5}$ for CIP was positively correlated with the degradation rate constant of CIP in the system of $LFPBC_{0.5}$/PMS, indicating that the adsorption performance of the material effectively promoted CIP degradation. Coexisting radical oxidation ($O_2^{\bullet-}$) and nonradical pathways ($^1O_2$ and electron transfer) in the $LFPBC_{0.5}$/PMS system were responsible for CIP degradation. Active sites identification revealed that Fe(II) in $LFPBC_{0.5}$ were the key species for PMS activation. Notably, further analysis demonstrated that phosphorus incorporation significantly enhanced the electron transfer rate and PMS adsorption capacity of $LFPBC_{0.5}$, along with an increase in the Fe(II) content of the material. Toxicity assessments indicated reduced toxicity of CIP degradation intermediates, confirming the

* Corresponding author.
E-mail address: 20200582@m.scnu.edu.cn (Y. Yi).

https://doi.org/10.1016/j.biortech.2026.134324
Received 15 December 2025; Received in revised form 13 February 2026; Accepted 28 February 2026
Available online 1 March 2026

environmental safety of the $LFPBC_{0.5}$/PMS system. This study presents an effective strategy for utilizing lithium-extraction residues while mitigating antibiotic contamination in water.

1. Introduction

Driven by the global carbon neutrality strategy, the new energy vehicle industry has experienced rapid development (Qin et al., 2026). By the end of 2025, China's annual production and sales of new energy vehicles had exceeded ten million units, with a market share surpassing 50% (Chen et al., 2025). With the widespread adoption of electric vehicles, the volume of end-of-life power batteries has also increased annually, and the cumulative retired quantity is projected to reach 820,000 tons by the end of 2025 (Hou et al., 2025). Therefore, developing recycling and comprehensive utilization technologies for retired power batteries is imperative to achieve high-value recovery of resources.

$LiFePO_4$ batteries have strong competitiveness in the market owing to their long cycle life, high safety, and cost-effectiveness (Shan et al., 2024). Given the high value and scarcity of lithium, recycling spent $LiFePO_4$ batteries primarily focuses on recovering lithium from the cathode material, leading to the generation of lithium-extraction residues, mainly composed of iron phosphate ($FePO_4$) (Forte et al., 2021). The high-value utilization of these lithium-extraction residues has long been a research focus. Numerous studies, both domestically and internationally, have explored the high-value utilization of these residues. For instance, Yang et al. found that the resulting cathode material derived from lithium-extraction residues exhibited an initial discharge capacity of 157.6 $mAh{\cdot}g^{-1}$ at 0.1C (Yang et al., 2024). He et al. demonstrated sulfide-induced phosphorus dissolution to directly recover phosphorus from the residues, achieving a recovery rate close to 100% within 5 h (He et al., 2020). Additionally, Wang et al. reported the successful removal of sulfamethoxazole within 30 min via PMS activation using pretreated spent $LiFePO_4$ cathode material (Wang et al., 2022). Guo et al. converted waste $FePO_4$ residue into oxalic acid-modified porous iron oxyhydroxide phosphate, which degraded 98.87% of Rhodamine B (RhB) within 15 min by activating H_2O_2 (Guo et al., 2022). However, the recycling of lithium-extraction residues still faces challenges such as high costs, energy consumption, and metal ion leaching, which limit further practical application. Therefore, it is crucial to explore more economical and environmentally friendly approaches to achieve the high-value utilization of these residues.

In recent years, magnetic biochar has been recognized as an important category of multifunctional environmental materials owing to its dual advantages derived from both biochar and magnetic properties (Yi et al., 2020). For example, Rong et al. confirmed that magnetic biochar could effectively activate persulfate, leading to the complete removal of bisphenol-A (Rong et al., 2019). Similarly, Ma et al. reported that magnetic biochar, prepared from waste red mud via co-pyrolysis, removed 99.7% of sulfadiazine within 20 min (Ma et al., 2022). Previous studies have shown that the preparation of magnetic biochar typically requires ferrous sulfate, potassium ferrate, or iron-containing wastes (Diao et al., 2021; Liu et al., 2019; Yi et al., 2021). Given that the main component of lithium-extraction residues is $FePO_4$, they could be utilized for the preparation of magnetic biochar, which is theoretically feasible and offers economic advantages over magnetic biochar prepared from conventional iron salts. Additionally, the in-situ incorporation of phosphorus not only enhances the adsorption performance of the material but also modulates the electron cloud density of the carbon framework, thereby improving its electron transfer capacity (Li et al., 2024). For instance, Liang et al. demonstrated that the introduction of phosphorus enhanced the electron storage and transfer capabilities of magnetic biochar, which resulted in efficient activation of PMS and highly effective degradation of 2-methyl-4-chlorophenoxyacetic acid in water (Liang et al., 2024). Unfortunately, limited research has explored the combination of lithium-extraction residues with agricultural and forestry waste biomass for the preparation of magnetic biochar. Furthermore, the effectiveness and mechanisms of the advanced oxidation systems constructed therefrom for removing organic pollutants from water remain unclear. This includes how iron and phosphorus components affect the iron redox cycle and electron transfer behavior during PMS activation.

In this study, magnetic biochar ($LFPBC_{0.5}$) was synthesized from lithium-extraction residues and rice straw via an impregnation-pyrolysis method, and coupled with PMS to degrade CIP in aqueous solution. The research primarily focused on the following aspects: (1) the physicochemical properties of $LFPBC_{0.5}$ were characterized; (2) the removal efficiency of CIP by $LFPBC_{0.5}$/PMS system was evaluated; (3) the key reactive oxygen species (ROS) and their contributions to CIP removal were identified; (4) the mechanism of PMS activation by $LFPBC_{0.5}$ for CIP degradation was thoroughly investigated; (5) the critical role of phosphorus in enhancing the performance of $LFPBC_{0.5}$ was verified; (6) CIP degradation pathways and the potential ecotoxicity of its degradation intermediates were investigated.

2. Materials and methods

2.1. Materials and reagents

All chemicals used in the experiments are of analytical grade and are listed in the supplementary material. The lithium-extraction residue, generated after lithium recovery from retired $LiFePO_4$ batteries, was obtained from Jiangxi Jiujiang Tinci High-New Material Co., Ltd. Rice straw was collected from a farm in Linyi, Shandong Province. Ultrapure water, produced using an RO-EDI system (resistivity 18.25 $M\Omega{\cdot}cm^{-1}$), was used throughout the study.

2.2. Catalyst preparation

The lithium-extraction residue (200 mesh) and rice straw biomass (100 mesh) were thoroughly mixed at mass ratios of 0.5:1, 1:1, and 2:1 (residue-to-biomass). Magnetic biochar was synthesized via an impregnation-pyrolysis method and designated as $LFPBC_{0.5}$, $LFPBC_1$, and $LFPBC_2$, correspondingly. Each mixture was dispersed in 200 mL of ultrapure water and magnetically stirred for 3 h at room temperature. After centrifugation, the supernatant was removed, and the solid residue was vacuum-dried at 80 °C for 12 h. The dried mixture was subsequently heated in a muffle furnace to 700 °C at a heating rate of 10 $°C{\cdot}min^{-1}$ and maintained at that temperature for 1.5 h. The resulting product was ground and sieved through a 100-mesh sieve. For comparison, rice straw and lithium-extraction residue were separately pyrolyzed under identical conditions to produce BC and LFP, respectively. Additionally, a conventional magnetic biochar, designated $FBC_{0.5}$, was prepared by mixing $FeSO_4{\cdot}7H_2O$ with rice straw biomass at the same mass ratio as a reference material.

2.3. Characterization methods

The microscopic morphology and elemental composition were examined using scanning electron microscopy with energy-dispersive X-ray spectroscopy (SEM-EDS, TESCAN MIRA LMS, Czech Republic) equipped with an OXFORD Xplore detector. Raman spectroscopy (WITec alpha300R, Germany) was employed to evaluate the defect density and structural disorder. The specific surface area and pore size distribution were measured with a fully automated surface area and porosity analyzer (Micromeritics ASAP 2460, USA) based on the

Brunauer-Emmett-Teller (BET) method. Crystal structure was characterized by X-ray diffraction (XRD, Rigaku SmartLab SE, Japan). Surface elemental composition and chemical states before and after the reaction were analyzed by X-ray photoelectron spectroscopy (XPS, Thermo Scientific K-Alpha, USA). Functional groups were qualitatively identified using Fourier transform infrared spectroscopy (FT-IR, Thermo Fisher Scientific Nicolet iN10, USA). The operation details of some characterization items can be found in the literature (Wang et al., 2025; Yao et al., 2025).

2.4. Experimental procedure

All experiments were conducted in a constant-temperature shaker at 25 °C and 200 rpm to maintain stable conditions throughout. For adsorption tests, a 10 $mg{\cdot}L^{-1}$ CIP solution was placed in a 150 mL sealed conical flask along with a predetermined amount of catalyst. At specified intervals, samples were taken with a syringe, filtered through a 0.22 μm membrane, and quenched with an equal volume of sodium thiosulfate to stop the reaction. The residual CIP concentration was then analyzed. The catalytic oxidation experiments followed the same procedure, except that a certain amount of PMS was added at the start, with no pre-adsorption equilibrium steps required.

To identify reactive species, quenching experiments employed methanol (MeOH), *tert*-butanol (TBA), p-benzoquinone (p-BQ), and L-histidine. The effect of pH was studied by adjusting the initial solution pH with 0.1 M acetic acid or sodium hydroxide. Potential interference from coexisting substances was evaluated by introducing anions or natural organic matter (NOM) at specific concentrations. Catalyst stability and reusability were tested by collecting the material after each run, washing it alternately with ultrapure water and ethanol, drying it, and then reusing it under identical conditions. The system's applicability was assessed using environmental water samples. All experiments included blanks and replicates to ensure reproducibility.

2.5. Analysis and computational methods

The detection methods for CIP and other pollutants are detailed in the supplementary material. The removal efficiencies of CIP via adsorption and degradation were calculated using the formulas provided in the supplementary material, with experimental data fitted to a first-order kinetic model. ROS and persistent free radicals (PFRs) were detected by an electron paramagnetic resonance (EPR) spectrometer (Bruker EMX PLUS, Germany) using 2,2,6,6-tetramethylpiperidine (TEMP) and dimethyl sulfoxide (DMPO) (100 mM each) as trapping agents. Electrochemical impedance spectroscopy (EIS) and chronoamperometry (i-t) measurements were conducted on an electrochemical workstation (Chenhua CHI-760E, China), as detailed in the supplementary material. Leaching concentrations of Fe(II) and total iron were determined by the phenanthroline method, while phosphate concentration was measured via the ammonium molybdate spectrophotometric method. PMS concentration changes were monitored spectrophotometrically using potassium iodide. The oxidative degradation products of CIP were analyzed by a liquid chromatography-tandem mass spectrometer (LC-MS/MS, Thermo Ultimate 3000 UHPLC-Q Exactive, USA), and their toxicity was assessed with the Toxicity Estimation Software Tool (T.E.S.T.). LC-MS/MS parameters, along with computational details for density functional theory (DFT) calculations, are included in the supplementary material.

3. Results and discussion

3.1. Catalyst characterization analysis

3.1.1. SEM-EDS

The morphologies and structures of the materials were characterized using SEM. BC showed a bundled porous structure with a smooth, dense surface, whereas LFP exhibited irregular aggregated granules. $LFPBC_{0.5}$ retained the tubular porous framework of BC along with granular LFP features (see supplementary material), with abundant particles on its surface providing reactive sites (Yang et al., 2023). Surface elemental analysis via energy-dispersive X-ray spectroscopy indicated iron and phosphorus contents of 9.48% and 6.07% in $LFPBC_{0.5}$ (see supplementary material), confirming successful incorporation of both elements. Elemental mapping further revealed a uniform dispersion of iron and phosphorus across the carbon matrix surface and pores (see supplementary material). This homogeneous distribution increased active site availability, promoting subsequent catalytic reactions (Zeng et al., 2022).

3.1.2. XRD

The crystalline structures of the materials were characterized by XRD (Fig. 1a). The XRD pattern of the pristine BC showed distinct diffraction peaks at $2\theta = 28.3^{\circ}$, 40.5°, 50.1°, 58.6°, 66.3°, and 73.7°. These peaks were indexed to the (200), (220), (222), (400), (420), and (422) planes of KCl (PDF#41–1476), respectively. This suggests that non-volatilized KCl was retained within the biochar during the pyrolysis of rice straw biomass (Deng et al., 2018). For the LFP sample, diffraction peaks observed at $2\theta = 20.4^{\circ}$, 25.7°, 35.7°, 38.1°, 41.4°, 48.6°, 58.4°, and 65.7° corresponded to the (100), (012), (110), (104), (200), (114), (212), and (124) planes of $FePO_4$ (PDF#72–2124), indicating $FePO_4$ as the primary phase. Notably, the XRD pattern of $LFPBC_{0.5}$ showed that except for a weak peak corresponding to the (012) plane of $FePO_4$, all other characteristic peaks disappeared. Concurrently, the diffraction intensities of the (322) and (040) planes of Fe_3O_4 increased slightly, suggesting the pyrolysis process facilitated the formation of Fe_3O_4. Furthermore, new diffraction peaks appeared at $2\theta = 20.4^{\circ}$, 31.8°, 34.6°, 36.2°, 44.2°, and 50.0°, which were consistent with $Fe_3(PO_4)_2$ (PDF#81–0694). This transformation was likely due to abundant reducing gases (e.g., CO, H_2, or biomass pyrolysis gases) generated during pyrolysis (Sun et al., 2019), which promoted the reduction of $FePO_4$ to the lower-valence iron oxide $Fe_3(PO_4)_2$. These results indicate the successful incorporation of both iron and phosphorus into the biochar. The iron species in the magnetic biochar primarily existed as $Fe_3(PO_4)_2$ and Fe_3O_4.

3.1.3. BET

N_2 adsorption–desorption isotherms (Fig. 1b) revealed type IV isotherms with hysteresis loops for all samples (Wang et al., 2020a). $LFPBC_{0.5}$ exhibited a specific surface area of 133.04 $m^2{\cdot}g^{-1}$, exceeding that of BC (4.95 $m^2{\cdot}g^{-1}$) and LFP (4.36 $m^2{\cdot}g^{-1}$) by factors of 26.88 and 30.51, respectively. Its total pore volume (0.112 $cm^3{\cdot}g^{-1}$) was also 8.00 and 9.33 times larger than those of BC (0.014 $cm^3{\cdot}g^{-1}$) and LFP (0.012 $cm^3{\cdot}g^{-1}$). These results demonstrate that the co-introduction of Fe and P markedly optimized the pore structure. The incorporation of lithium-extraction residue effectively enhanced the specific surface area and porosity of the pristine biochar. This improvement likely originated from the co-pyrolysis of biomass with the residue, during which Fe components catalyzed biochar graphitization and volatile matter decomposition, thereby increasing surface area and pore volume. BJH-based pore size distribution analysis indicated a smaller average pore size for $LFPBC_{0.5}$ (6.997 nm) compared to BC (12.062 nm) and LFP (10.246 nm) (see supplementary material). During pyrolysis, phosphate bridges helped prevent pore collapse, while iron-containing phosphates immobilized oxidative groups on pore walls via catalytic oxidation, contributing to the reduced average pore size. The resulting abundant mesoporous structure facilitates the diffusion of pollutant molecules into the catalyst interior, promoting oxidant activation efficiency (Chu et al., 2019).

3.1.4. FT-IR

The surface functional groups of the materials were analyzed by FT-IR (Fig. 1c). All samples showed similar characteristic absorption peaks. The broad peak at 3432 cm^{-1} corresponds to O—H stretching vibrations

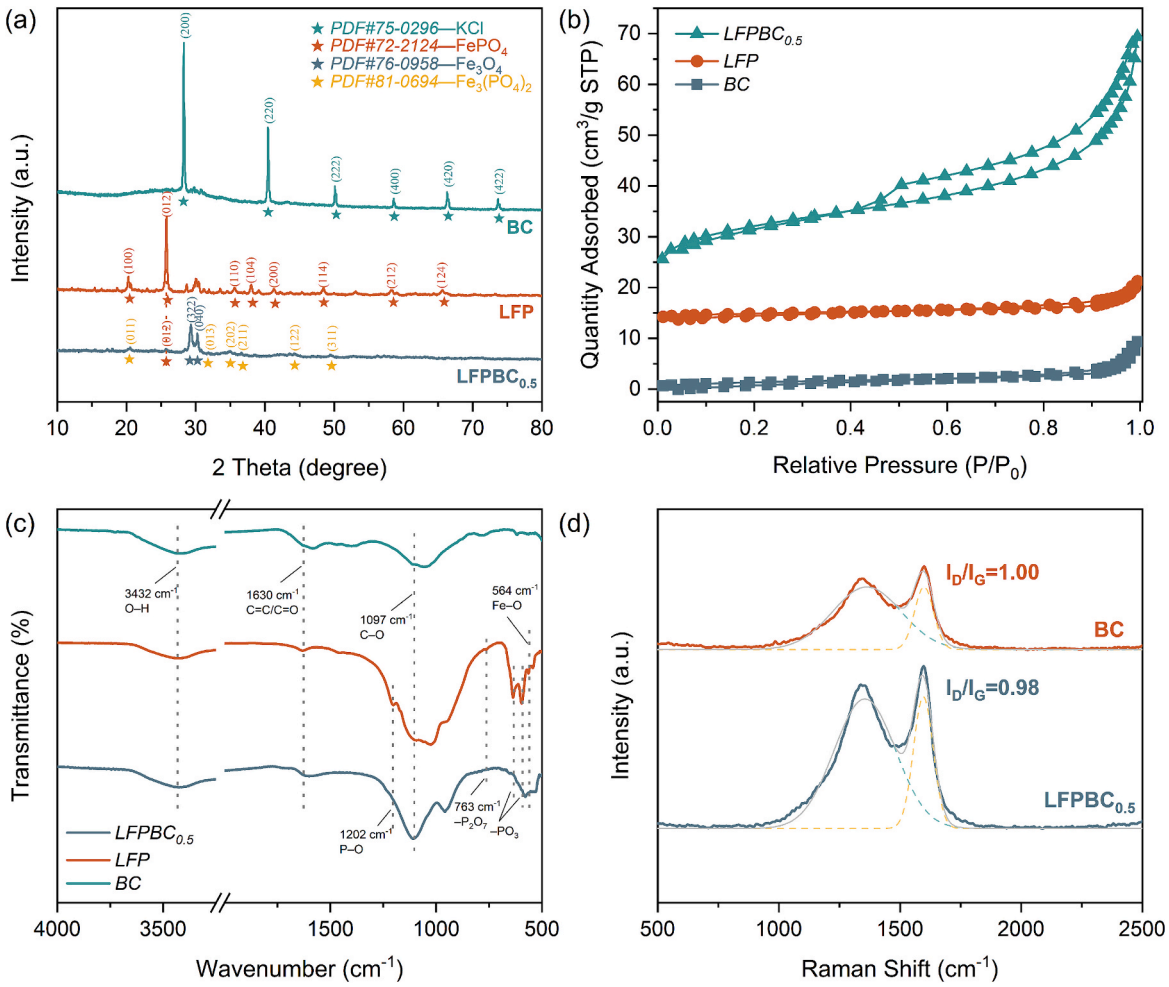

Fig. 1. (a) XRD spectra of different materials; (b) N_2 adsorption/desorption isotherms; (c) FT-IR spectral analysis of different materials; (d) Raman spectra of different materials.

(Fang et al., 2024), the peak at 1570 cm^{-1} to C═C/C═O stretching (Xu et al., 2024), and the peak at 1097 cm^{-1} to C—O stretching (Al Masud et al., 2023). Peaks specific to phosphorus species were observed only in LFP and $LFPBC_{0.5}$. These include the P—O bond at 1202 cm^{-1}, the $–P_2O_7$ group at 763 cm^{-1} (Liang et al., 2025a). Additionally, the peaks at 595 cm^{-1} and 635 cm^{-1} were assigned to the stretching vibrations of metaphosphate groups ($–PO_3$) (Guo et al., 2015). These characteristic peaks were not detected in the pristine biochar. Meanwhile, a distinct Fe–O stretching vibration at 564 cm^{-1} was also identified in LFP and $LFPBC_{0.5}$ (Luo et al., 2022). These findings indicate that $LFPBC_{0.5}$ possesses a greater diversity and abundance of surface oxygen-containing functional groups compared to pristine biochar.

3.1.5. Raman

Raman spectroscopy was employed to analyze the surface defects and graphitization degree of the materials. Characteristic peaks for the disordered carbon (D band, ~1346 cm^{-1}) and graphitic carbon (G band, ~1597 cm^{-1}) were clearly observed in both BC and $LFPBC_{0.5}$ (Fig. 1d). The calculated I_D/I_G ratio for $LFPBC_{0.5}$ (0.98) was lower than that for BC (1.00). This indicates a higher degree of graphitization and a more stable carbon structure in $LFPBC_{0.5}$, which is beneficial for interfacial charge transfer (Wang et al., 2020b). In contrast, the Raman spectrum of LFP was dominated by a strong peak at 1012 cm^{-1} (see supplementary material), assigned to the PO_4 stretching mode of non-bridging oxygen (Zhang & Brow, 2011). Several lower-intensity peaks were also observed in the range between 200 and 500 cm^{-1}, and the spectral features were consistent with those of α-$FePO_4$.

3.2. Effect of initial conditions on CIP removal

3.2.1. Catalyst dosage

The practical engineering application of catalysts is constrained by removal efficiency and economic cost. This study investigated how catalyst dosage affects CIP removal (Fig. 2a). Increasing the dosage from 0.1 to 1.0 $g{\cdot}L^{-1}$ enhanced CIP removal efficiency from 30.66% to 89.77% and raised the apparent rate constant (k_{obs}) from 0.0041 to 0.0253 min^{-1}. At a constant PMS concentration, a higher catalyst dosage supplies more available active sites. This promotes the generation of reactive species, thereby improving CIP degradation (Shaoyi et al., 2023).

3.2.2. PMS concentration

The concentration of PMS is another key factor affecting system efficiency (Fig. 2b). With the catalyst dosage fixed at 1.0 $g{\cdot}L^{-1}$, CIP removal efficiencies reached 84.34% and 84.99% at PMS concentrations of 0.5 and 1.0 mM, respectively. Increasing PMS to 2.0 mM further improved removal to 89.77%. These results indicate that higher PMS concentrations within this range enhanced antibiotic degradation by promoting the generation of reactive species, thereby increasing their attack on CIP molecules (Shaoyi et al., 2023). However, when PMS was increased further to 2.5 mM, CIP removal decreased to 84.18% and the k_{obs} value dropped from 0.0253 to 0.0205 min^{-1}. This decline may result from excess PMS causing overproduction and subsequent self-quenching of radicals, which inhibits degradation (Bo et al., 2023).

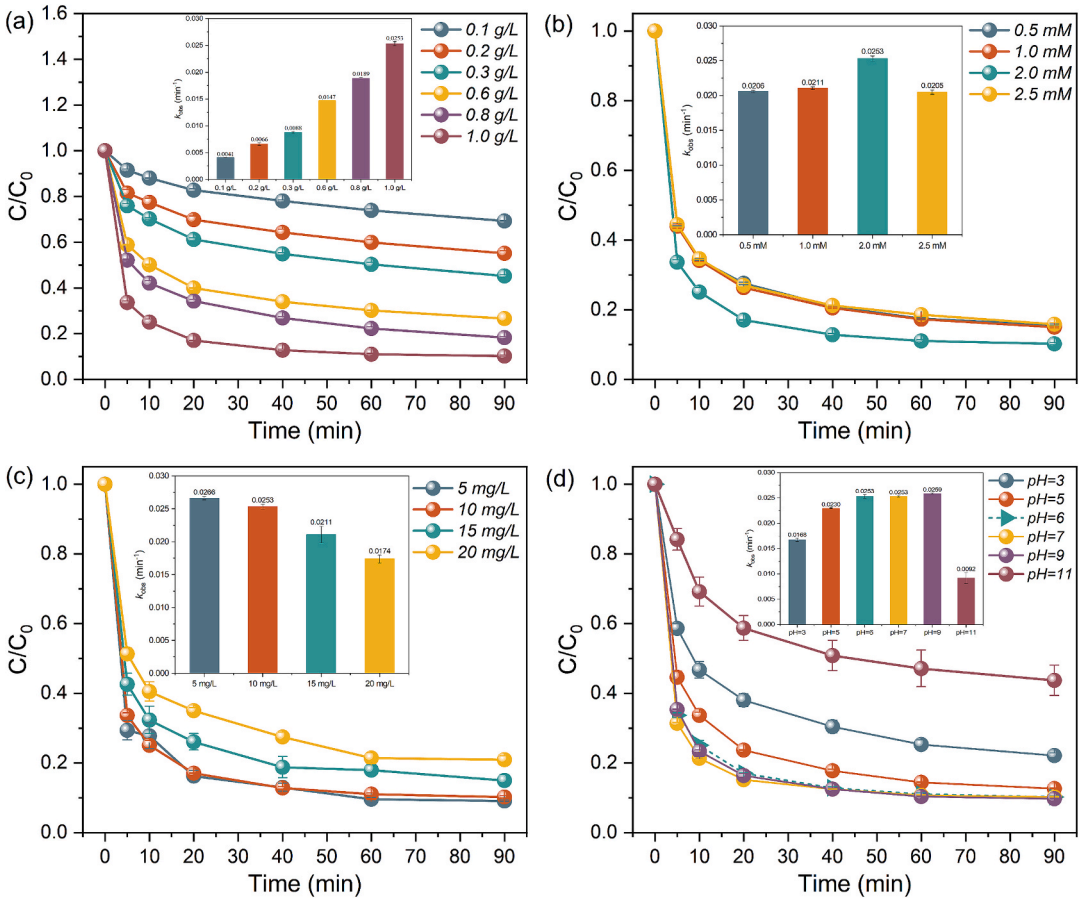

Fig. 2. Effect of process parameter optimization on CIP degradation efficiency: (a) catalyst dosage; (b) PMS dosage; (c) CIP concentration; (d) environmental pH. (Reaction conditions: $[LFPBC_{0.5}]_0$ = 0.1–1.0 g·L^{-1}, $[PMS]_0$ = 0.5–2.5 mM, $[CIP]_0$ = 5–20 mg·L^{-1}, pH = 3–11).

3.2.3. *Initial CIP concentration*

The influence of initial CIP concentration on system performance was examined (Fig. 2c). Efficient removal of CIP was achieved within 90 min at concentrations of 5–10 mg·L^{-1}. However, as the initial concentration increased from 10 mg·L^{-1} to 15 mg·L^{-1} and 20 mg·L^{-1}, the degradation efficiency decreased from 89.77% to 85.02% and 79.08%, respectively. This decline is likely due to the limited availability of active sites, oxidants, and reactive oxygen species in the system. Their finite oxidative capacity becomes insufficient to degrade higher concentrations of organic pollutant, leading to reduced removal efficiency (Deng et al., 2024).

3.2.4. *Initial solution pH*

The initial solution pH significantly influenced the activation of PMS by $LFPBC_{0.5}$ for CIP degradation (Fig. 2d). The $LFPBC_{0.5}$/PMS system demonstrated stable CIP removal across a wide pH range (3–9). However, at pH 11, the degradation was significantly suppressed, with removal efficiency dropping to 56.30%. To elucidate the mechanisms behind the reduced degradation efficiency under strongly acidic (pH = 3) and alkaline (pH = 11) conditions, the point of zero charge (pH_{pzc}) of $LFPBC_{0.5}$ was determined. The pH_{pzc} was approximately 6.19 (see supplementary material). Since CIP exists predominantly as anionic CIP^- above pH 8.7 (see supplementary material), under alkaline conditions (pH > pH_{pzc}), both the catalyst surface and CIP^-/HSO_5^- are negatively charged. The resulting electrostatic repulsion reduces their adsorption onto the catalyst, lowering removal efficiency. Beyond adsorption effects, the sharp decline at high pH may also relate to the stability of reactive species. In highly alkaline environments, PMS undergoes self-decomposition, reducing oxidant availability. Furthermore, reactive oxygen species can react with excess OH^- to form less reactive products like SO_4^{2-}, weakening overall oxidative capacity. Under highly acidic conditions (pH < pH_{pzc}), the high H^+ concentration may scavenge reactive species or inhibit their generation, further impairing system performance (Liang et al., 2025a).

3.3. *Adsorption and activation performance of the catalyst*

The structural formation of the catalyst during preparation was modulated by varying the component ratios, which subsequently governed its pollutant adsorption and catalytic performance. As illustrated in Fig. 3a, sole LFP and BC removed 10.06% and 22.16% of CIP within 90 min, respectively. The composite $LFPBC_{0.5}$ exhibited the highest adsorption capacity, achieving 69.15% CIP removal in 90 min with an adsorption rate constant K of 0.0131 min^{-1}. This value was 10.92 times that of LFP (0.0012 min^{-1}) and 4.68 times that of BC (0.0028 min^{-1}) (Fig. 3b). Further increasing the mass ratio of lithium-extraction residue to rice straw reduced adsorption efficiency to 55.60% for $LFPBC_1$ and 40.61% for $LFPBC_2$. This decline corresponded to changes in material structure. SEM images indicated that $LFPBC_{0.5}$ contained lithium-extraction residue particles attached to its surface, increasing its specific surface area and total pore volume. It can be inferred that a higher residue proportion gradually blocks the pore structure of the magnetic biochar, reducing available adsorption sites. Notably, PMS alone showed limited oxidative ability, removing only 4.28% of CIP. When PMS was added to systems containing BC, LFP, or $LFPBC_{0.5}$, CIP removal improved markedly (Fig. 3c). The $LFPBC_{0.5}$/PMS system performed best, with 89.77% removal (k_{obs} = 0.0253 min^{-1}) (Fig. 3d), corresponding to a 1.30-fold enhancement over $LFPBC_{0.5}$ alone. The BC/PMS and LFP/PMS systems removed 56.14% (k_{obs} = 0.0092 min^{-1}) and 38.56% (k_{obs} = 0.0054 min^{-1}) of CIP, representing 2.53-fold and 3.83-fold increases

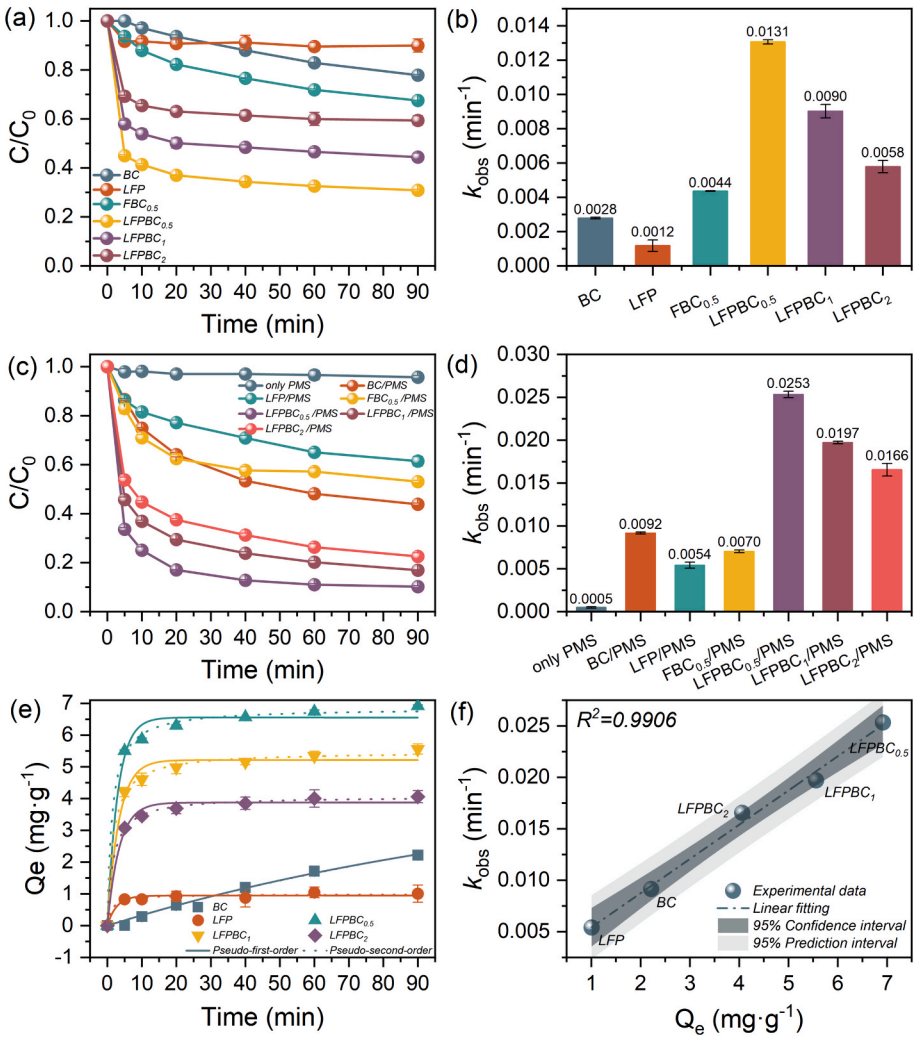

Fig. 3. (a) Adsorption efficiency of CIP on different catalysts; (b) k_{obs} for CIP adsorption on different catalysts; (c) Degradation performance of CIP in different systems; (d) k_{obs} for CIP degradation in different systems; (e) Adsorption kinetic curves and fitting for CIP adsorption by different catalysts; (f) Correlation between the k_{obs} and the equilibrium adsorption capacity Q_e for different catalysts. (Reaction conditions: $[CIP]_0$ = 10 mg·L^{-1}, $[Catalyst]_0$ = 1.0 g·L^{-1}, $[PMS]_0$ = 2 mM, pH = 6).

relative to their PMS-free counterparts. However, increasing the mass ratio of lithium-extraction residue to rice straw ($LFPBC_1$ and $LFPBC_2$) did not further enhance the catalytic activity. Instead, the CIP removal efficiencies decreased to 83.21% and 78.51%, respectively. Given the reported role of phosphorus in promoting catalytic activity, a phosphorus-free magnetic biochar ($FBC_{0.5}$) was prepared using commercial ferrous sulfate. $FBC_{0.5}$ alone adsorbed 32.56% of CIP, while the $FBC_{0.5}$/PMS system increased removal by only 14.88%, with a k_{obs} of 0.0070 min^{-1}, much lower than that of $LFPBC_{0.5}$/PMS (0.0253 min^{-1}). This contrast confirms that in-situ phosphorus incorporation optimizes the pore structure of biochar and elevates its graphitization degree, thereby introducing more active sites and accelerating oxidation. These results align with prior reports that P-doping enhances graphitization and electron transfer (Wang et al., 2023), underscoring the vital role of phosphorus in boosting system catalysis.

The synergistic effect between adsorption and oxidation processes has been demonstrated to significantly enhance pollutant removal efficiency, surpassing individual adsorption or oxidation pathways (Liang et al., 2025b). To clarify the inherent relationship between the adsorption performance of the catalysts and their ability to catalytically degrade CIP, the adsorption behavior of CIP on different catalysts was evaluated using pseudo-first-order and pseudo-second-order kinetic models (Fig. 3e). The fitting results indicated that the pseudo-second-order kinetic model exhibited higher correlation coefficients (see supplementary material), suggesting that the adsorption of CIP onto the catalyst surface was predominantly governed by chemical adsorption mechanisms. To further identify the rate-controlling step of the adsorption process, an intraparticle diffusion model was applied for analysis (see supplementary material). Initially, CIP rapidly diffused through the boundary layer to the active sites on the catalyst surface, followed by intraparticle diffusion into the internal pores, eventually reaching diffusion-adsorption equilibrium (see supplementary material). This indicated that both liquid-film diffusion and intraparticle diffusion jointly governed the adsorption process. Notably, the intraparticle diffusion model showed a relatively poor fit for LFP, implying that this step was not the primary rate-controlling mechanism for its adsorption. To distinguish the roles of adsorption and oxidation, the residual CIP proportion in solution (f_{aq}) and on the catalyst (f_{ad}) was quantified, and the oxidized fraction (f_{oxid}) was calculated by difference (see supplementary material). In the $LFPBC_{0.5}$/PMS system, f_{ad}, f_{aq}, and f_{oxid} reached 11%, 10%, and 79%, respectively, confirming that CIP adsorbed onto $LFPBC_{0.5}$ was further oxidized by ROS generated from PMS activation. Moreover, a strong positive correlation (R^2 = 0.9906) was observed between the equilibrium adsorption capacity (Q_e) of the catalysts and the apparent rate constant (k_{obs}) of degradation (Fig. 3f). This result verifies that the adsorption capability of the catalyst

effectively facilitated the subsequent catalytic degradation of CIP in the LFPBC$_{0.5}$/PMS system. In summary, LFPBC$_{0.5}$ exhibited the optimal adsorption-catalysis synergy and was therefore selected as the primary material for further mechanistic investigation.

3.4. Removal mechanism of CIP in the LFPBC$_{0.5}$/PMS system

3.4.1. Identification and scavenging of reactive free radicals

To elucidate the reaction mechanism of the LFPBC$_{0.5}$/PMS system and identify the dominant ROS, free radical quenching experiments and EPR spectroscopy were employed. EPR analysis revealed the coexistence of multiple ROS. Using DMPO as a spin-trapping agent, distinct signals for DMPO–•OH and DMPO–$SO_4^{\bullet-}$ adducts were detected (Fig. 4b), with hyperfine splitting constants (α) of approximately 14.95 G and 14.47 G, respectively. The characteristic signal of DMPO–$O_2^{\bullet-}$ was also observed (Fig. 4c). Notably, the intensities of all three radical adducts increased continuously over time, indicating sustained radical generation. Furthermore, when TEMP was used as a specific trap for $^1O_2$, a characteristic 1:1:1 triplet signal was recorded (Fig. 4d), with an α value of about 17.30 G (Villamena et al., 2008), confirming the presence of $^1O_2$. This signal also showed a significant time-dependent increase.

To clarify the roles of ROS in the reaction, radical scavenging experiments were performed. MeOH, which quenches both sulfate radicals ($SO_4^{\bullet-}$, k = (1.6–7.7) × 10^7 $M^{-1}s^{-1}$) and hydroxyl radicals (•OH, k = (1.2–2.8) × 10^9 $M^{-1}s^{-1}$), and TBA, a selective •OH scavenger (k = (3.8–7.6) × 10^9 $M^{-1}s^{-1}$), caused only slight inhibition of CIP degradation at 10 mM (Gao et al., 2022) (Fig. 4a). Corresponding EPR still showed a clear DMPO–•OH signal, possibly due to the chosen quencher concentration, indicating that •OH and $SO_4^{\bullet-}$ played a limited, non-dominant role. In contrast, adding 10 mM L-Histidine (a $^1O_2$ scavenger, k = 3.2 × 10^7 $M^{-1}s^{-1}$) markedly reduced CIP degradation to 41.23% within 90 min, confirming $^1O_2$ as the primary oxidative species.

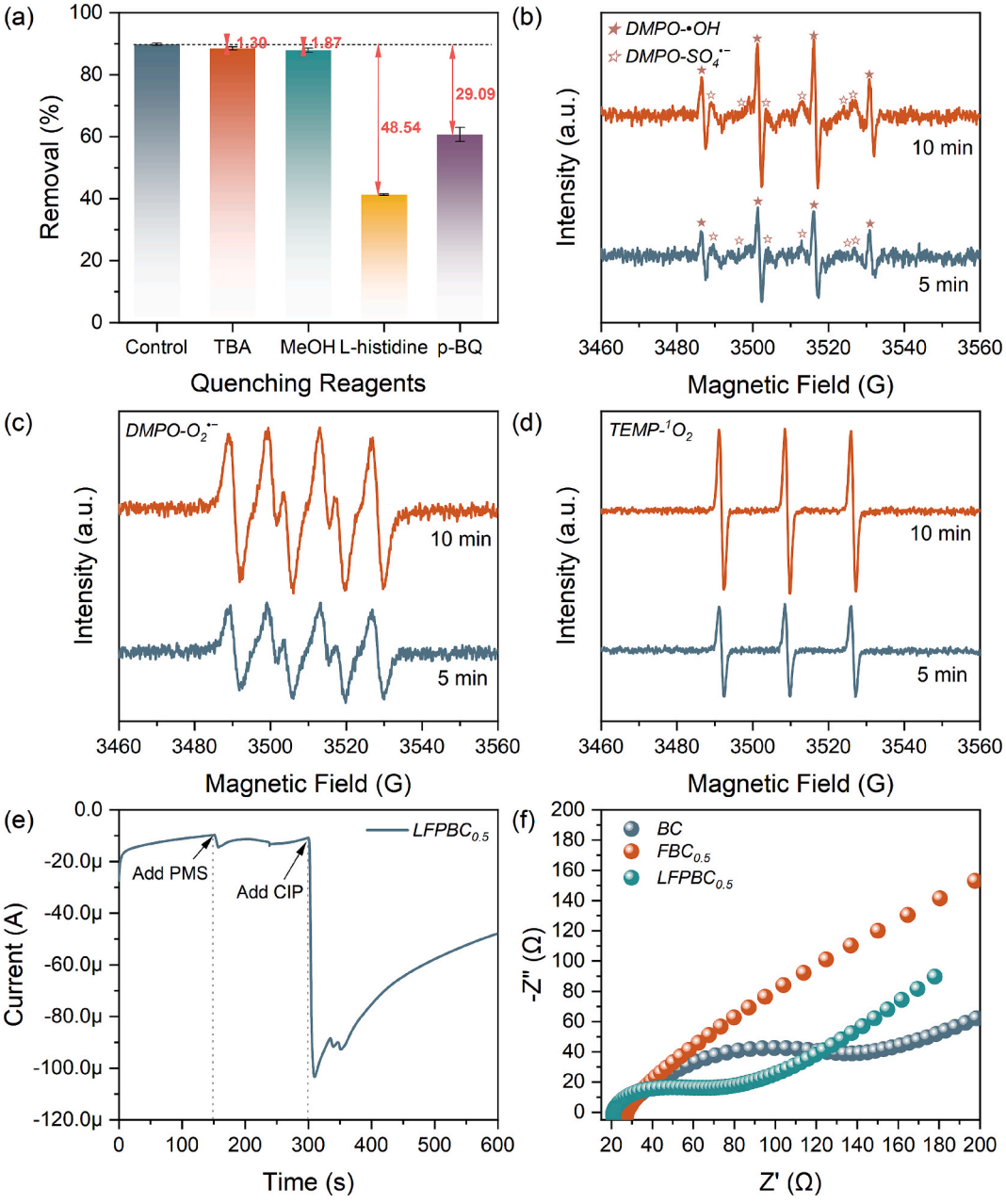

Fig. 4. (a) Quenching experiment of the LFPBC$_{0.5}$/PMS system; (b-d) EPR spectra of •OH and $SO_4^{\bullet-}$, $O_2^{\bullet-}$ and $^1O_2$; (e) Chronoamperometric curves of LFPBC$_{0.5}$ after adding PMS and CIP; (f) EIS curves of BC, FBC$_{0.5}$, and LFPBC$_{0.5}$.

Furthermore, p-BQ (an $O_2^{\bullet-}$ scavenger, $k = 2.9 \times 10^9\ M^{-1}s^{-1}$) lowered the removal efficiency to 60.68%, demonstrating a significant contribution from superoxide radicals ($O_2^{\bullet-}$). When N_2 was purged to remove dissolved oxygen, CIP removal decreased from 89.77% to 73.57%, underscoring the importance of O_2 in generating $O_2^{\bullet-}$ (see supplementary material). Given that $O_2^{\bullet-}$ is a known precursor to $^1O_2$, these results suggest that both $O_2^{\bullet-}$ and $^1O_2$ are key reactive species in the system, likely interconnected through a transformation pathway (Zhu et al., 2025). Based on the quenching results, the relative contributions were calculated to be 46.40% for the radical pathway and 53.60% for the non-radical pathway, with $^1O_2$ identified as the predominant reactive species throughout the process.

3.4.2. *Identification of active sites*

To clarify the surface chemical evolution of the catalyst during the reaction and its correlation with catalytic activity, spent $LFPBC_{0.5}$ was characterized by XPS. All spectra were charge-corrected using the C 1s peak at 284.8 eV as a reference before peak fitting. The XPS survey spectrum indicated notable changes in the relative contents of Fe and P after the reaction (see supplementary material), suggesting these species may be directly involved in activating PMS and degrading CIP.

The high-resolution C 1s spectrum (Fig. 5a) revealed that the surface carbon species of fresh $LFPBC_{0.5}$ primarily consisted of C—C/C═C (284.8 eV), C—O (286.4 eV), C═O (288.8 eV), a π–π* satellite peak (295.9 eV), and a hybrid K 2p peak (293.0 eV), with relative contents of 57.46%, 18.99%, 14.68%, 2.18%, and 6.69%, respectively. After the reaction, the relative content of C—O decreased, while that of C═O increased slightly. Notably, the π–π* satellite peak decreased from 2.18% to 1.47%. This reduction can be attributed to π–π stacking interactions between CIP molecules and the porous carbon structure of the catalyst (Jiang et al., 2023), further confirming the strong adsorption capacity of $LFPBC_{0.5}$ toward CIP.

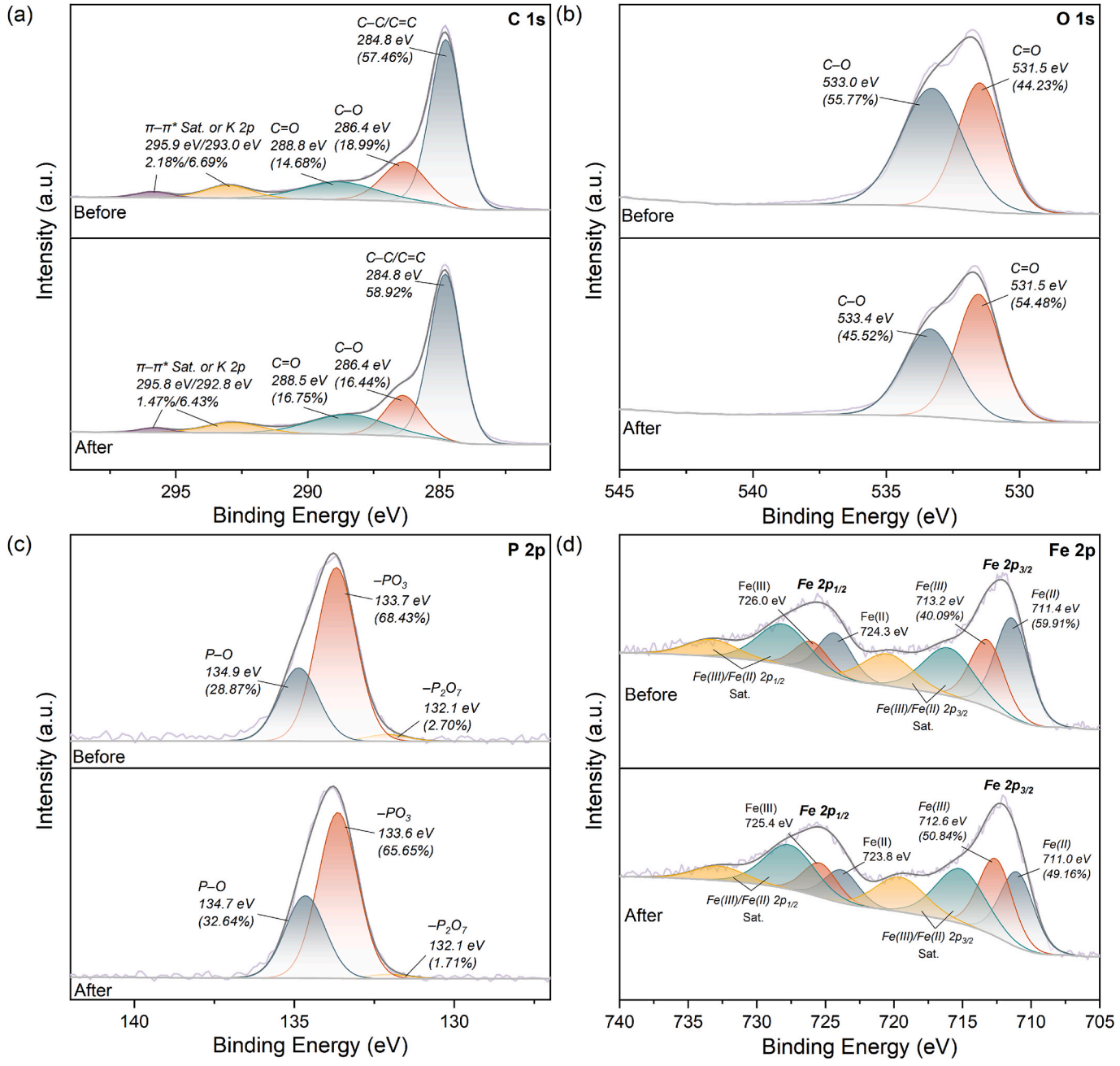

Fig. 5. XPS spectra of $LFPBC_{0.5}$ before and after reaction: (a) C 1 s, (b) O 1 s, (c) P 2p, (d) Fe 2p.

The O 1s spectrum (Fig. 5b) showed two characteristic peaks corresponding to C═O (531.5 eV) and C—O (533.0 eV). Their relative contents changed after the reaction, which may be linked to the adsorption of PMS and CIP on the catalyst surface.

The high-resolution P 2p spectrum (Fig. 5c) was fitted with three components corresponding to $–P_2O_7$ (132.1 eV), $–PO_3$ (133.7 eV), and P—O (134.9 eV). After the reaction, the P—O content increased to 32.64%. This increase is attributed to the positively charged graphitized phosphorus atoms, which favor the adsorption of anionic CIP (Liang et al., 2024). The decrease in $–P_2O_7$ content likely resulted from its masking in solution through hydrogen-bond interactions (Liang et al., 2025a). Meanwhile, $–PO_3$ can act as an electron donor to facilitate the reduction of Fe(III) to Fe(II) (Huang et al., 2023), thereby enhancing PMS activation and pollutant degradation. These changes were supported by FT-IR spectra (see supplementary material). The vibrational peaks for the $–P_2O_7$ group (763 cm^{-1}), C—O (1097 cm^{-1}), and $–PO_3$ were weakened after the reaction. This indicates that the phosphorus-containing functional groups introduced during synthesis played a key role in enriching both PMS and CIP on the catalyst surface. Additionally, the enhanced O—H stretching vibration is likely due to the formation of Fe–OH species during the reaction (Liang et al., 2024), which may contribute to ROS generation.

The Fe 2p region exhibited the most notable changes (Fig. 5d). Peaks at 710.8 eV and 723.9 eV were assigned to Fe(II) 2p3/2 and Fe(II) 2p1/2, respectively, while those at 713.2 eV and 726.5 eV corresponded to Fe(III). After the reaction, the Fe(II) content decreased from 59.91% to 49.16%, with a corresponding increase in Fe(III) from 40.09% to 50.84%. This confirms that Fe redox cycling was crucial for activating PMS and degrading CIP, which is consistent with the 70.26% PMS consumption observed in the system (see supplementary material). Quenching experiments further verified the key role of iron valence states (Peng et al., 2024). Adding the Fe(II) chelator 1,10-phenanthroline (5 $mg{\cdot}L^{-1}$) reduced the CIP degradation rate to 46.01%, indicating that Fe(II) deactivation directly impaired PMS activation. Similarly, adding the Fe(III) chelator EDTA-2Na (1 mM) lowered the degradation rate to 52.90% (see supplementary material). These results directly demonstrate that Fe(II) serves as the primary active species for PMS activation, and an intact Fe(II)/Fe(III) cycle is essential for sustaining high catalytic efficiency.

PFRs on carbon materials can serve as potential single-electron transfer sites during persulfate activation. To probe their role, BC and $LFPBC_{0.5}$ were analyzed by EPR. Both materials showed a broad singlet signal at $g \approx 2.003$, characteristic of carbon-centered PFRs generated during pyrolysis (see supplementary material). The PFRs signal was significantly more intense for $LFPBC_{0.5}$ than for BC, indicating that iron and phosphorus doping promoted PFRs formation. To assess the actual contribution of PFRs in catalysis, $LFPBC_{0.5}$ was pretreated with methanol to selectively quench surface PFRs (Xie et al., 2024). After quenching, CIP degradation efficiency decreased only marginally by 6.89% (see supplementary material). This result suggests that although PFRs are present, their role in the overall degradation process is limited and not the dominant mechanism.

In summary, Fe species are considered the primary active sites in $LFPBC_{0.5}$ for PMS activation. The Fe(II)/Fe(III) redox cycle drives the process by continuously activating PMS to generate ROS. Meanwhile, phosphorus-containing functional groups (PFGs) not only provide adsorption sites that enrich organic pollutants, but also significantly promote the iron redox cycle, thereby enhancing catalytic efficiency synergistically.

3.4.3. The role of P in enhancing catalyst performance

To understand how phosphorus introduction improves the catalyst's bonding structure and performance, the high-resolution XPS spectra of $FBC_{0.5}$ and $LFPBC_{0.5}$ were compared (see supplementary material). Both materials showed hybrid K 2p peaks, likely originating from KCl in the rice straw biomass. Notably, the relative content of the π–π* satellite peak in $LFPBC_{0.5}$ (2.18%) was significantly higher than that in $FBC_{0.5}$ (0.91%), which correlated positively with the catalyst's adsorption performance. This suggests phosphorus introduction effectively enhanced the surface adsorption capacity. Furthermore, the Fe(II) content in $LFPBC_{0.5}$ (59.91%) was higher than that in $FBC_{0.5}$ (57.61%), indicating that phosphorus doping promoted the elevation of Fe(II) content, thereby facilitating the Fe(II)/Fe(III) redox cycle.

Phosphorus doping can optimize the electronic structure of catalysts and promote electron transfer (Huang et al., 2023). To investigate the electron-transfer pathways between the catalyst, oxidant, and pollutant, EIS was performed. The Nyquist plots (Fig. 4f) revealed that $LFPBC_{0.5}$ possessed the smallest semicircle radius in the high-frequency region, indicating the lowest charge-transfer resistance and the highest electrical conductivity. This confirms that phosphorus doping significantly enhanced the electron transport capability of the material. Furthermore, when potassium dichromate ($K_2Cr_2O_7$) was added as an exogenous electron acceptor, the CIP degradation efficiency decreased progressively with increasing $K_2Cr_2O_7$ concentration (see supplementary material). This result indirectly suggests the presence of a non-radical electron-transfer pathway in the $LFPBC_{0.5}$/PMS/CIP system. To directly monitor the current response, chronoamperometry (i-t) tests were conducted using an $LFPBC_{0.5}$-coated electrode (Fig. 4e). The current remained stable with $LFPBC_{0.5}$ alone. After PMS addition, a slight current fluctuation indicated initial PMS activation. Upon introducing CIP, the current increased markedly, confirming that CIP acts as an electron donor. This establishes an efficient electron-transfer channel with PMS adsorbed on the catalyst surface as the electron acceptor, sustaining interfacial electron transfer and accelerating the redox reaction.

3.4.4. DFT analysis

DFT calculations elucidated the intrinsic mechanism by which P introduction influences the catalyst performance. The possible structures of Fe-BC and Fe/P-BC, along with their top and side views, are displayed in the supplementary material. The adsorption energy (E_{ads}) of PMS on Fe/P-BC was −1.98 eV, which was significantly enhanced compared to that on Fe-BC (−0.62 eV). This result indicated that the incorporation of P markedly improved the chemical adsorption capacity of the material for PMS, thereby further promoting the generation of $^1O_2$ and the degradation of CIP.

To further analyze the electronic structure changes after PMS adsorption, the most stable adsorption configurations were constructed, and the charge density difference (CDD) was calculated for Fe-BC and Fe/P-BC. In the CDD diagrams, the yellow regions represent electron concentration, while the blue cyan regions indicate electron dissipation. The results revealed that when PMS was adsorbed on the single Fe-based material surface (see supplementary material), electron depletion occurred around the Fe atoms, whereas the adsorbed PMS molecule exhibited electron accumulation. It is noteworthy that in P-containing Fe/P-BC, the O atom adjacent to S in the PMS molecule preferentially adsorbed onto the P site. This suggests that PMS tends to bind more readily with the electron-deficient phosphorus center rather than the electron-deficient carbon center (Di et al., 2025). Such an adsorption pattern represents a key initial step for activating PMS. Furthermore, the incorporation of phosphorus optimized the electronic structure of the material surface, promoting electron transfer between the catalyst and PMS. Consequently, the activation efficiency of PMS and the pollutant degradation performance were effectively enhanced.

3.4.5. Possible removal mechanisms of CIP

Based on the above discussion, a removal mechanism for CIP in the $LFPBC_{0.5}$/PMS system is proposed (Fig. 6).

1. The co-introduction of Fe and P synergistically optimized the pore structure and specific surface area of $LFPBC_{0.5}$, providing abundant sites for PMS activation. Simultaneously, PMS and CIP were pre-concentrated via electrostatic attraction and π–π interactions,

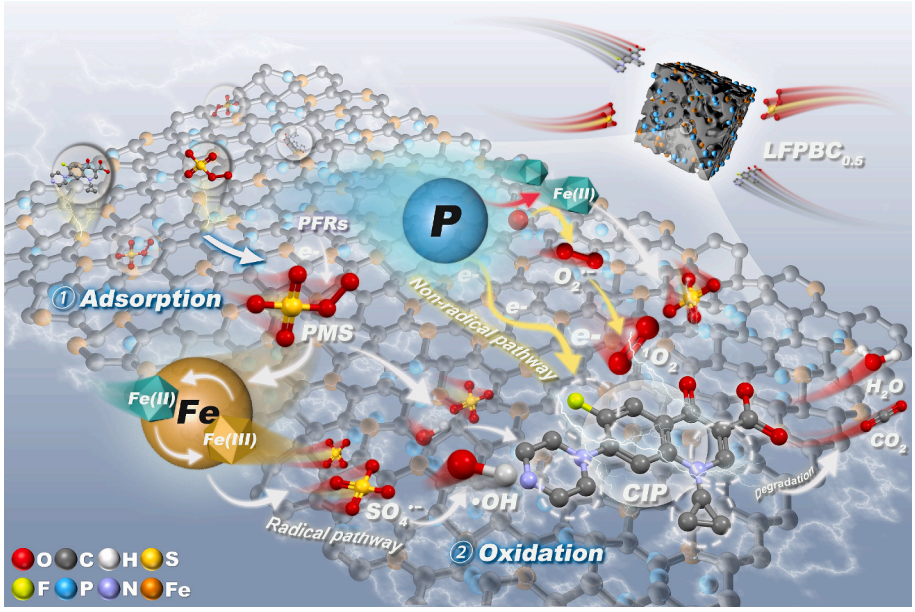

Fig. 6. Possible mechanism for CIP removal in the $LFPBC_{0.5}$/PMS system.

respectively, increasing local reactant concentrations. Surface phosphorus-containing groups further enhanced adsorption. XPS analysis revealed a rise in P—O bond content after reaction, likely because P-induced local positive charge centers favored adsorption of anionic CIP species or PMS. The $-P_2O_7$ groups could also act as hydrogen-bond acceptors, strengthening CIP adsorption. These groups were partially covered/transformed during the reaction, decreasing their content to 1.71%. Previous studies confirm that effective adsorption on carbon carriers shortens the diffusion distance to ROS, reducing non-target consumption (Ding et al., 2020). Moreover, compared with P-free $FBC_{0.5}$, phosphorus incorporation significantly improved charge-transfer efficiency between iron species and the biochar. EIS results showed $LFPBC_{0.5}$ had the lowest charge-transfer resistance and highest conductivity, indicating that P promotes electron migration. This enhanced electron conduction not only facilitated PMS activation to generate ROS but may also enable direct electron-transfer oxidation of CIP.

2. The surface enrichment of PMS and CIP on $LFPBC_{0.5}$ promoted their contact with Fe(II) active sites. Fe(II) primarily activated PMS via single electron transfer to produce $SO_4^{\bullet-}$ (Equation (1)). $SO_4^{\bullet-}$ could further react with H_2O to form •OH (Equation (2)) (Liang et al., 2024). Meanwhile, PFRs in $LFPBC_{0.5}$ directly donated electrons to PMS, supplementing radicals for CIP attack (Equation (3)). In addition, dissolved oxygen could also accept electrons from the Fe(II)/Fe(III) cycle, being reduced to $O_2^{\bullet-}$ (Equation (4)), which then disproportionated into $^1O_2$ (Equation (5)). Together, these ROS formed the oxidative system for CIP degradation. Crucially, in-situ P incorporation played a dual role in promoting the oxidation process. Firstly, it increased the initial Fe(II) content in $LFPBC_{0.5}$. Secondly, $-PO_3$ groups acted as electron donors, efficiently reducing Fe(III) to Fe(II). This sustained and accelerated the Fe(II)/Fe(III) redox cycle (Equation (6)) (Liang et al., 2025a), ensuring continuous PMS activation. Ultimately, CIP was effectively degraded through combined adsorptive enrichment and multi-pathway oxidation (Equation (7)).

$$Fe(II) + HSO_5^- \rightarrow Fe(III) + SO_4^{\bullet-} + OH^- \quad (1)$$

$$SO_4^{\bullet-} + H_2O \rightarrow SO_4^{2-} + \bullet OH + H^+ \quad (2)$$

$$PFRs + e^- + HSO_5^- \rightarrow SO_4^{\bullet-} + \bullet OH \quad (3)$$

$$Fe(II) + O_2 \rightarrow Fe(III) + O_2^{\bullet-} \quad (4)$$

$$2O_2^{\bullet-} + 2H^+ \rightarrow {}^1O_2 + H_2O_2 \quad (5)$$

$$Fe(III) + HSO_5^- \rightarrow Fe(II) + SO_5^{\bullet-} + H^+ \quad (6)$$

$$ROS + CIP \rightarrow Intermediates + CO_2 + H_2O \quad (7)$$

3.5. Intermediates and toxicity assessment

3.5.1. Degradation pathway of CIP in the $LFPBC_{0.5}$/PMS system

LC-MS/MS was used to identify possible degradation intermediates of CIP. Based on the mass-to-charge ratios (m/z) of detected standards, fourteen potential intermediates were identified (see supplementary material). Two main degradation pathways were proposed, namely piperazine ring opening (Pathway I) and deacetylation (Pathway II) (Zeng et al., 2024). In Pathway I, the piperazine ring of CIP (D0, m/z 332) was attacked by reactive species (e.g., $SO_4^{\bullet-}$), leading to oxidative ring opening and formation of a dialdehyde derivative D1 (m/z 362). D1 underwent decarbonylation to yield D2 (m/z 334), followed by deamination and dealkylation to form D3 (m/z 291). Sequential loss of carbonyl, amino and alkyl groups converted D3 into D4 (m/z 263). Subsequent carbon–nitrogen bond cleavage and cycloalkane removal generated D5 (m/z 223), which was defluorinated to D6 (m/z 205). Alternatively, D5 could undergo oxidative cleavage of the quinolone ring to produce D7 (m/z 200). Further removal of amino and carboxyl groups converted D7 into D8 (m/z 112), and finally deamination yielded small molecules such as D9 (m/z 94). In Pathway II, CIP first underwent defluorination, possibly with hydroxyl substitution, to form D10 (m/z 330). D10 could be attacked by radicals, resulting in dehydroxylation and piperazine ring opening to yield D11 (m/z 344). Alternatively, D10 could be directly transformed into D13 (m/z 273) via sequential decarbonylation, deamination and dealkylation. D13 was further converted to intermediate D6 through decarbonylation and cycloalkane removal. The intermediates generated in both pathways subsequently underwent ring opening, oxidation and other reactions, ultimately mineralizing into carbon dioxide, water, fluoride ions and other small inorganic molecules, thereby achieving complete CIP removal.

3.5.2. Toxicity assessment of CIP degradation products

The ecotoxicity of transformation products generated during CIP degradation was assessed via T.E.S.T. software (see supplementary material). Most intermediates displayed lower acute toxicity to *Daphnia magna* than CIP, except D4. Notably, certain products exhibited higher developmental toxicity, which declined as degradation progressed. Predictions for bioconcentration factor (BCF) and mutagenicity were also obtained. CIP showed a BCF of 10.95. Most intermediates had lower values, but D9 reached 24.50, which was 2.24 times that of CIP. Mutagenicity was detected only in D1, D5, and D8 (Pathway I) and in D10, D11, and D13 (Pathway II). Overall, the $LFPBC_{0.5}$/PMS system effectively converted CIP into products with reduced ecotoxicity, though some remain environmentally concerning. Mineralization was evaluated by total organic carbon analysis, confirming that only partial mineralization of CIP was achieved under optimal conditions (see supplementary material).

Phytotoxicity was examined using a wheat germination assay. While seed germination and shoot growth were normal in treated water, root growth was significantly inhibited (see supplementary material). This inhibition was similar to that of the original CIP solution, suggesting the formation of intermediates with developmental toxicity to plants, consistent with software predictions (Zhang et al., 2022). Thus, although the system degrades CIP and allows partial mineralization with minimal effect on shoots, the presence of toxic intermediates warrants further treatment to ensure complete ecological safety.

3.6. Effect of complex environmental conditions on CIP degradation

3.6.1. Anions and natural organic matter

Common coexisting substances in natural water, including anions (SO_4^{2-}, Cl^-, HCO_3^-, $H_2PO_4^-$) and natural organic matter such as humic acid (HA), can compete for reactive sites or oxidizing species and thus interfere with CIP removal (see supplementary material). The addition of 5 mM SO_4^{2-} slightly reduced CIP removal from 89.77% to 88.72%, indicating negligible inhibition likely due to limited site blocking. Cl^- also caused a modest decrease in overall degradation efficiency. Notably, in the presence of Cl^-, the system showed a significantly faster CIP degradation rate within the first 20 min ($k_{obs} = 0.0930\ min^{-1}$). This acceleration is attributed to the reaction of Cl^- with $SO_4^{\bullet-}$ and •OH, generating reactive chlorine species with higher oxidation potentials such as Cl•, $Cl_2^{\bullet-}$, and HOCl (Equations (8)-(12)) (Wang & Wang, 2021). However, this promoting effect was unsustainable due to the limited total radical concentration. In contrast, HCO_3^- considerably suppressed degradation, lowering CIP removal to 82.40%, mainly because it scavenges $SO_4^{\bullet-}$ and •OH to form less reactive HCO_3• and $CO_3^{\bullet-}$ (Equations (13)-(14)) (Zeng et al., 2024). $H_2PO_4^-$ exhibited only weak inhibition, which was also negligible. Furthermore, increasing HA concentration to 1 and 5 $mg{\cdot}L^{-1}$ reduced CIP removal to 86.13% and 85.15%, respectively. This decline likely results from HA competing with the catalyst for active sites, thereby hindering the synergistic adsorption-oxidation process. Overall, the $LFPBC_{0.5}$/PMS system demonstrated strong resistance to environmental interference.

$$SO_4^{\bullet-} + Cl^- \rightarrow Cl^{\bullet} + SO_4^{2-} \quad (8)$$

$$Cl^- + Cl^{\bullet} \rightarrow Cl_2^{\bullet-} \quad (9)$$

$$\bullet OH + Cl^- \rightarrow ClOH^{\bullet-} \quad (10)$$

$$ClOH^{\bullet-} + Cl^- \rightarrow OH^- + Cl_2^{\bullet-} \quad (11)$$

$$Cl^- + HSO_5^- \rightarrow HOCl + SO_4^{2-} \quad (12)$$

$$SO_4^{\bullet-} + HCO_3^- \rightarrow SO_4^{2-} + H^+ + CO_3^{\bullet-} \quad (13)$$

$$\bullet OH + HCO_3^- \rightarrow SO_4^{2-} + H_2O + CO_3^{\bullet-} \quad (14)$$

3.6.2. Salt concentration

High salinity, a common but challenging feature of industrial wastewater, often severely inhibits advanced oxidation processes. To assess the feasibility of the $LFPBC_{0.5}$/PMS system under such conditions, CIP degradation was evaluated across a wide NaCl concentration range (2.5–20 wt%) (see supplementary material). Compared to the salt-free control, the final CIP removal efficiency was only slightly inhibited. Notably, at an extremely high salinity of 20 wt%, the removal efficiency (85.72%) even exceeded that at 2.5 wt% (80.29%), indicating a non-monotonic response to salt concentration. More importantly, during the initial 10-minute reaction phase, the observed rate constant (k_{obs}) for all salt-containing groups was higher than that of the control. This early stage enhancement aligns with the previously discussed role of Cl^-, confirming that high chloride concentrations continuously participate in the reaction, generating highly reactive chlorine species (e.g., Cl•, $Cl_2^{\bullet-}$, and HOCl) and thus accelerating early phase degradation. However, at the highest salinity (20 wt%), the sharply increased solution viscosity became the dominant limiting factor. This effect hindered the mass transfer of PMS and CIP molecules to the catalyst's active sites, moderately suppressing the generation of $SO_4^{\bullet-}$/•OH radicals and their subsequent reactions with CIP.

3.6.3. Natural water

To evaluate the applicability and robustness of the $LFPBC_{0.5}$/PMS system in real aquatic environments, CIP degradation was tested in three typical natural water samples (see supplementary material). The system showed effective resistance to interference and remained stable across different water matrices. Degradation efficiency was comparable in the control group (89.77%) and tap water (89.61%), followed by lake water (87.83%), with river water exhibiting the lowest removal (82.40%). This variation is mainly due to water matrix components, particularly the higher NOM content in river water. Phenolic and quinoid moieties in NOM likely scavenge reactive oxidative species, partially reducing oxidation efficiency.

3.6.4. Other pollutants

To evaluate the universality of the oxidative capability of the $LFPBC_{0.5}$/PMS system, representative organic pollutants including norfloxacin, tetracycline hydrochloride, and RhB were selected for degradation experiments (see supplementary material). The removal efficiencies for all target pollutants exceeded 90.0%. The results demonstrate that the $LFPBC_{0.5}$/PMS system exhibited highly efficient and broad-spectrum degradation capability toward various common organic pollutants in water, which supports its potential application in actual wastewater treatment.

3.7. Stability and reusability

The environmental safety of catalysts depends on minimizing metal leaching. In the $LFPBC_{0.5}$/PMS system during CIP degradation, leaching of Fe(II) and total iron was monitored (see supplementary material). Both increased over time, reaching maximum concentrations of 0.22 $mg{\cdot}L^{-1}$ for Fe(II) and 0.27 $mg{\cdot}L^{-1}$ for total iron after 90 min. These values are substantially below the 5 $mg{\cdot}L^{-1}$ total iron limit specified by China's Integrated Wastewater Discharge Standard (GB 8978–1996). Total phosphorus release peaked at 0.59 $mg{\cdot}L^{-1}$ at 90 min, also below the standard's secondary discharge limit of 1.0 $mg{\cdot}L^{-1}$. In summary, while effectively degrading pollutants, the $LFPBC_{0.5}$/PMS system demonstrated good structural stability and a low secondary pollution risk.

Catalyst cycling stability is essential for practical application. The $LFPBC_{0.5}$/PMS system maintained 87.82% CIP removal after two cycles, but efficiency declined markedly to 51.04% by the fourth cycle (see supplementary material). This decrease was mainly due to the accumulation of CIP degradation products on active sites, which hindered

mass transfer, along with reduced pre-adsorption of PMS and CIP that gradually lowered ROS generation and catalytic activity. After reactivation by oxygen-limited recalcination at 400 °C, the used $LFPBC_{0.5}$ recovered a CIP degradation efficiency of 89.69% within 90 min (see supplementary material).

4. Conclusion

In this study, $LFPBC_{0.5}$ showed an excellent capacity in activating PMS for the degradation of CIP. CIP degradation in $LFPBC_{0.5}$/PMS system relied on the synergistic effects of both radical and non-radical pathways. Meanwile, Fe(II) in $LFPBC_{0.5}$ was recognized as the key active site for PMS activation. The incorporation of phosphorus significantly increased the adsorption capacity, electron transfer efficiency, and Fe(II) content of $LFPBC_{0.5}$, thereby promoting the effective degradation of CIP in the $LFPBC_{0.5}$/PMS system. Toxicity assessment confirmed that the toxicity of CIP oxidation products in the $LFPBC_{0.5}$/PMS system was reduced, and the system was less affected by factors such as co-existing anions, HA, and varying salt concentrations. In summary, this study provides new insights into the high-value resource utilization of lithium-extraction residues and the efficient removal of antibiotics from water.

CRediT authorship contribution statement

Yue Fu: Writing – original draft, Software, Methodology, Investigation, Formal analysis, Data curation. **Yunqiang Yi:** Writing – review & editing, Supervision, Funding acquisition, Formal analysis. **Weirui Chen:** Writing – review & editing, Software. **Yu Wang:** Writing – review & editing. **Zenghui Diao:** Writing – review & editing. **Jianying Qi:** Writing – review & editing.

Declaration of competing interest

The authors declare that they have no known competing financial interests or personal relationships that could have appeared to influence the work reported in this paper.

Acknowledgments

The study were supported by National Natural Science Foundation of China (42107395), Young Talent Support Project of Guangzhou Association for Science and Technology (QT2024-013), Guangzhou Science and Technology Plan Project (2025A04J4231), Special Projects in Key Fields of Ordinary Universities in Guangdong Province (2024ZDZX4011), Innovation Team Project for Ordinary Universities of Guangdong Province (2024KCXTD007), Modern Agricultural Industrial Technology System of Guangdong Province (2024CXTD18).

Appendix A. Supplementary data

Supplementary data to this article can be found online at https://doi.org/10.1016/j.biortech.2026.134324.

Data availability

Data will be made available on request.

References

Al Masud, M.A., Shin, W.S., Kim, D., 2023. Fe-doped kelp biochar-assisted peroxymonosulfate activation for ciprofloxacin degradation: Multiple active site-triggered radical and non-radical mechanisms. Chem. Eng. J. 471. https://doi.org/10.1016/j.cej.2023.144519.

Bo, J., Yunshu, Z., Cong, L., Jiaqi, G., Chunmeng, S., 2023. Zero-valent iron loaded on N-doped biochar fabricated by one-step pyrolysis of K_2FeO_4 and coffee grounds as a persulfate activator for bisphenol a degradation. Process Saf. Environ. Prot. 170, 328–338. https://doi.org/10.1016/j.psep.2022.11.081.

Chen, C.X., Wang, Q., Wang, X.F., Li, Y.J., Tian, S.L., Yuan, X., 2025. Photocatalysis-assisted one-step synthesis of ferrous pyrophosphate from retired lithium-iron phosphate batteries: a green route to the selective synthesis of anode materials. ACS Sustain. Chem. Eng. 13 (44), 19261–19270. https://doi.org/10.1021/acssuschemeng.5c08420.

Chu, C.H., Yang, J., Huang, D.H., Li, J.F., Wang, A.Q., Alvarez, P.J.J., Kim, J.H., 2019. Cooperative pollutant adsorption and persulfate-driven oxidation on hierarchically ordered porous carbon. Environ. Sci. Technol. 53 (17), 10352–10360. https://doi.org/10.1021/acs.est.9b03067.

Deng, L., Ye, J.M., Jin, X., Che, D.F., 2018. Transformation and release of potassium during fixed-bed pyrolysis of biomass. J. Energy Inst. 91 (4), 630–637. https://doi.org/10.1016/j.joei.2017.02.009.

Deng, Y., Xiao, L., Zhou, H., Cui, B., Zhang, L., Chen, D., Gu, C., Zhan, Z., Wang, R., Mei, S., Pei, X., Li, Q., Ye, Y., Pan, F., 2024. Phytic acid pre-modulated and Fe/N co-doped biochar derived from ramie fiber to active persulfate for efficient degradation of tetracycline via radical and non-radical pathways. Sep. Purif. Technol. 342. https://doi.org/10.1016/j.seppur.2024.126976.

Di, X.X., Zeng, X., Zhang, X.Y., Tang, T., Zhao, Z.P., Wang, W., Liu, Z.F., Jin, L.X., Ji, X. H., Shao, X.Z., 2025. Nitrogen-phosphorus codoped biochar prepared from tannic acid for degradation of trace antibiotics in wastewater. Environ. Res. 266. https://doi.org/10.1016/j.envres.2024.120589.

Diao, Z.H., Zhang, W.X., Liang, J.Y., Huang, S.T., Dong, F.X., Yan, L., Qian, W., Chu, W., 2021. Removal of herbicide atrazine by a novel biochar based iron composite coupling with peroxymonosulfate process from soil: synergistic effect and mechanism. Chem. Eng. J. 409. https://doi.org/10.1016/j.cej.2020.127684.

Ding, D.H., Zhou, L., Kang, F.X., Yang, S.J., Chen, R.Z., Cai, T.M., Duan, X.G., Wang, S.B., 2020. Synergistic adsorption and oxidation of ciprofloxacin by biochar derived from metal-enriched phytoremediation plants: experimental and computational insights. ACS Appl. Mater. Interfaces 12 (48), 53788–53798. https://doi.org/10.1021/acsami.0c15861.

Fang, J.R., He, F., Yan, Z.L., Wang, J.J., Yu, R., Zhou, H.H., 2024. Pyrite/biochar-activated peroxymonosulfate strengthens tetracycline degradation: important roles of surface functional groups and Fe(II)/Fe(III) redox cycling. J. Environ. Chem. Eng. 12 (3). https://doi.org/10.1016/j.jece.2024.112923.

Forte, F., Pietrantonio, M., Pucciarmati, S., Puzone, M., Fontana, D., 2021. Lithium iron phosphate batteries recycling: an assessment of current status. Crit. Rev. Environ. Sci. Technol. 51 (19), 2232–2259. https://doi.org/10.1080/10643389.2020.1776053.

Gao, Y.J., Chen, Y., Song, T.H., Su, R., Luo, J.C., 2022. Activated peroxymonosulfate with ferric chloride-modified biochar to degrade bisphenol A: characteristics, influencing factors, reaction mechanism and reuse performance. Sep. Purif. Technol. 300. https://doi.org/10.1016/j.seppur.2022.121857.

Guo, S., Zhang, G., Yu, J.C., 2015. Enhanced photo-Fenton degradation of rhodamine B using graphene oxide-amorphous $FePO_4$ as effective and stable heterogeneous catalyst. J. Colloid Interface Sci. 448, 460–466. https://doi.org/10.1016/j.jcis.2015.02.005.

Guo, W.L., Cao, Y., Zhang, Y., Wang, L.J., Kong, L.X., 2022. Synthesis of porous iron hydroxy phosphate from phosphate residue and its application as a Fenton-like catalyst for dye degradation. J. Environ. Sci. 112, 307–319. https://doi.org/10.1016/j.jes.2021.05.033.

He, K., Zhang, Z.Y., Zhang, F.S., 2020. A green process for phosphorus recovery from spent $LiFePO_4$ batteries by transformation of delithiated $LiFePO_4$ crystal into $NaFeS_2$. J. Hazard. Mater. 395. https://doi.org/10.1016/j.jhazmat.2020.122614.

Hou, S.Y., Yang, F., Zhuang, X.N., Song, X.L., Dou, Y.Q., Wu, W.J., 2025. The environmental impact and eco-efficiency analysis of retired power battery recycling in China. J. Energy Storage 120. https://doi.org/10.1016/j.est.2025.116483.

Huang, P., Zhang, P., Wang, C.P., Du, X., Jia, H.Z., Sun, H.W., 2023. P-doped biochar regulates nZVI nanocracks formation for superefficient persulfate activation. J. Hazard. Mater. 450. https://doi.org/10.1016/j.jhazmat.2023.130999.

Jiang, H.H., Hu, Z.X., Ouyang, Y.H., Ji, X.D., Hu, X., Li, T.T., Ouyang, K., Wang, P., Wang, H., Hu, X.J., 2023. Multi-phase CdS loaded on biochar for photocatalytic activation of peroxymonosulfate for thiamethoxam degradation: p-conjugation improves PMS adsorption. Sep. Purif. Technol. 326. https://doi.org/10.1016/j.seppur.2023.124842.

Li, R.Z., Zhang, C.Y., Hui, J., Shen, T.H., Zhang, Y., 2024. The application of P-modified biochar in wastewater remediation: a state-of-the-art review. Sci. Total Environ. 917. https://doi.org/10.1016/j.scitotenv.2024.170198.

Liang, X.T., Zhao, Y.J., Li, J.R., Liu, B.Y., Cui, Y.L., Hou, W.H., Xie, D.R., Liu, H.Z., Wang, H., Geng, P.H., Yang, Q., Yang, Z.L., 2025a. Phosphorus doping-induced electron transfer promotes cobalt-iron biochar activation of peracetic acid: selective reactive substance generation for pesticide degradation. Chem. Eng. J. 509. https://doi.org/10.1016/j.cej.2025.161468.

Liang, X.T., Zhao, Y.J., Liu, B.Y., Li, J.R., Cui, L.Y., Wang, C.Y., Yang, Q., 2024. Phosphorus doped magnetic biochar activated PMS for effective degradation of pesticide in water: targeted regulation of interfacial charge transfer by phosphorus doping. Sep. Purif. Technol. 340. https://doi.org/10.1016/j.seppur.2024.126739.

Liang, Y., Cui, J., Ning, C., Zhang, F., Liang, F., Gao, J., 2025b. Construction of adsorption-oxidation bifunction-oriented sludge biochar for non-radical ofloxacin degradation via persulfate: emphasizing the important role of N-species and graphitized structure. Sep. Purif. Technol. 354. https://doi.org/10.1016/j.seppur.2024.129239.

Liu, C., Chen, L.W., Ding, D.H., Cai, T.M., 2019. From rice straw to magnetically recoverable nitrogen doped biochar: efficient activation of peroxymonosulfate for

the degradation of metolachlor. Appl. Catal. B-Environ. 254, 312–320. https://doi.org/10.1016/j.apcatb.2019.05.014.
Luo, J., Yi, Y., Ying, G., Fang, Z., Zhang, Y., 2022. Activation of persulfate for highly efficient degradation of metronidazole using Fe(II)-rich potassium doped magnetic biochar. Sci. Total Environ. 819. https://doi.org/10.1016/j.scitotenv.2021.152089.
Ma, D.M., Wang, J., Feng, K., Liu, B.F., Xie, G.J., Xing, D.F., 2022. A green strategy from waste red mud to Fe^0-based biochar for sulfadiazine treatment by peroxydisulfate activation. Chem. Eng. J. 446. https://doi.org/10.1016/j.cej.2022.136944.
Peng, Y.F., Xue, C.J., Luo, J.Y., Zheng, B., Fang, Z.Q., 2024. Lanthanum-doped magnetic biochar activating persulfate in the degradation of florfenicol. Sci. Total Environ. 916. https://doi.org/10.1016/j.scitotenv.2024.170312.
Qin, T.X., Zhang, Q., Su, X., Tan, X.C., Jin, H., Ye, W.T., Zhao, B., 2026. A review and prospects of research on coordinated optimization operation of energy stations. Renew. Sust. Energ. Rev. 229. https://doi.org/10.1016/j.rser.2025.116625.
Rong, X., Xie, M., Kong, L.S., Natarajan, V., Ma, L., Zhan, J.H., 2019. The magnetic biochar derived from banana peels as a persulfate activator for organic contaminants degradation. Chem. Eng. J. 372, 294–303. https://doi.org/10.1016/j.cej.2019.04.135.
Shan, M.H., Dang, C.Y., Meng, K., Cao, Y.T., Zhu, X.Q., Zhang, J., Xu, G.Y., Zhu, M.F., 2024. Recycling of $LiFePO_4$ cathode materials: from laboratory scale to industrial production. Mater. Today 73, 130–150. https://doi.org/10.1016/j.mattod.2023.12.012.
Shaoyi, Z., Kunquan, L., Xia, X., Jiayong, Z., Yan, X., 2023. Efficiently catalytic degradation of tetracycline via persulfate activation with plant-based biochars: insight into endogenous mineral self-template effect and pyrolysis catalysis. Chemosphere 337, 139309. https://doi.org/10.1016/j.chemosphere.2023.139309.
Sun, Y.H., Zhao, Q., Luo, C.H., Wang, G.X., Sun, Y., Yan, K.P., 2019. A novel strategy for the synthesis of $Fe_3(PO_4)_2$ using Fe-P waste slag and CO_2 followed by its use as the precursor for $LiFePO_4$ preparation. ACS Omega 4 (6), 9932–9938. https://doi.org/10.1021/acsomega.9b01074.
Villamena, F.A., Liu, Y.P., Zweier, J.L., 2008. Superoxide radical anion adduct of 5,5-dimethyl-1-pyrroline N-oxide. 4. Conformational effects on the EPR hyperfine splitting constants. Chem. A Eur. J. 112 (49), 12607–12615. https://doi.org/10.1021/jp8070579.
Wang, C., Holm, P.E., Andersen, M.L., Thygesen, L.G., Nielsen, U.G., Hansen, H.C.B., 2023. Phosphorus doped cyanobacterial biochar catalyzes efficient persulfate oxidation of the antibiotic norfloxacin. Bioresour. Technol. 388. https://doi.org/10.1016/j.biortech.2023.129785.
Wang, H., Cao, Y.Z., Li, B.S., Shen, L.G., Wu, X.L., Li, R.J., Lin, H.J., 2025. Photothermal nano-confinement reactor with bimetallic sites for enhanced peroxymonosulfate activation in antibiotic degradation. Water Res. 268. https://doi.org/10.1016/j.watres.2024.122623.
Wang, H.Z., Guo, W.Q., Liu, B.H., Si, Q.S., Luo, H.C., Zhao, Q., Ren, N.Q., 2020a. Sludge-derived biochar as efficient persulfate activators: Sulfurization-induced electronic structure modulation and disparate nonradical mechanisms. Appl. Catal. B-Environ. 279. https://doi.org/10.1016/j.apcatb.2020.119361.
Wang, J.L., Wang, S.Z., 2021. Effect of inorganic anions on the performance of advanced oxidation processes for degradation of organic contaminants. Chem. Eng. J. 411. https://doi.org/10.1016/j.cej.2020.128392.
Wang, K., Sun, Y., Tang, J., He, J., Sun, H., 2020b. Aqueous Cr(VI) removal by a novel ball milled Fe^0-biochar composite: role of biochar electron transfer capacity under high pyrolysis temperature. Chemosphere 241. https://doi.org/10.1016/j.chemosphere.2019.125044.
Wang, P., Lou, X.Y., Chen, Q.Q., Liu, Y.J., Sun, X.H., Guo, Y.G., Zhang, X.J., Wang, R.X., Wang, Z.H., Chen, S., Zhang, L., Zhang, R.Q., Guan, J., 2022. Spent $LiFePO_4$: an old but vigorous peroxymonosulfate activator for degradation of organic pollutants in water. Environ. Res. 214. https://doi.org/10.1016/j.envres.2022.113780.
Xie, J., Latif, J., Yang, K.J., Wang, Z.Q., Zhu, L., Yang, H.Q., Qin, J.J., Ni, Z., Jia, H.Z., Xin, W., Li, X., 2024. A state-of-art review on the redox activity of persistent free radicals in biochar. Water Res. 255. https://doi.org/10.1016/j.watres.2024.121516.
Xu, M., Wu, J.S., Wang, J.S., Zhou, W.Y., Li, Y.L., Li, H.Y., 2024. Bamboo leaf-derived biochar/iron silicate composite for an adsorption-degradation synergistic removal of ciprofloxacin. Process Saf. Environ. Prot. 186, 1183–1196. https://doi.org/10.1016/j.psep.2024.04.074.
Yang, L.Y., Wang, D.D., Zhang, J.L., Chen, Y.Q., Wang, C.Y., 2024. An economical and closed-loop hydrometallurgical method to prepare battery-grade iron phosphate from delithiated $LiFePO_4$ cathode scrap. J. Clean. Prod. 444. https://doi.org/10.1016/j.jclepro.2024.141194.
Yang, Z.H., An, Q., Deng, S.M., Xu, B.H., Li, Z., Deng, S., Zhao, B., Ye, Z.H., 2023. Efficient activation of peroxydisulfate by modified red mud biochar derived from waste corn straw for levofloxacin degradation: efficiencies and mechanisms. J. Environ. Chem. Eng. 11 (6). https://doi.org/10.1016/j.jece.2023.111609.
Yao, X.Y., Li, R.J., Shen, L.G., Zhao, L.H., Lin, H.J., 2025. A novel magnetically induced Co@NC-modified electrochemical membrane for continuous peroxymonosulfate activation: achieving ultrafast and cost-effective purification with elucidation of mechanism and application potential. Water Res. 287. https://doi.org/10.1016/j.watres.2025.124436.
Yi, Y.Q., Huang, Z.X., Lu, B.Z., Xian, J.Y., Tsang, E.P., Cheng, W., Fang, J.Z., Fang, Z.Q., 2020. Magnetic biochar for environmental remediation: a review. Bioresour. Technol. 298. https://doi.org/10.1016/j.biortech.2019.122468.
Yi, Y.Q., Tu, G.Q., Ying, G.G., Fang, Z.Q., Tsang, E.P., 2021. Magnetic biochar derived from rice straw and stainless steel pickling waste liquor for highly efficient adsorption of crystal violet. Bioresour. Technol. 341. https://doi.org/10.1016/j.biortech.2021.125743.
Zeng, H.P., Li, J.X., Xu, J.X., Qi, W., Hao, R.X., Gao, G.W., Lin, D., Li, D., Zhang, J., 2022. Preparation of magnetic N-doped iron sludge based biochar and its potential for persulfate activation and tetracycline degradation. J. Clean. Prod. 378. https://doi.org/10.1016/j.jclepro.2022.134519.
Zeng, J., Gao, T.Z., Li, Z., Lin, J., Zhu, Y.X., Li, D., Ke, F.M., Gao, D., Wang, D.D., 2024. Magnetic recyclable g-C_3N_4/$CuFe_2O_4$/MnO_2 activated peroxymonosulfate process via dual Z-scheme heterojunction for photodegradation of ciprofloxacin. J. Environ. Chem. Eng. 12 (6). https://doi.org/10.1016/j.jece.2024.114502.
Zhang, H.Q., Quan, H.T., Yin, S.Z., Sun, L.P., Lu, H., 2022. Unraveling the toxicity associated with ciprofloxacin biodegradation in biological wastewater treatment. Environ. Sci. Technol. 56 (22), 15941–15952. https://doi.org/10.1021/acs.est.2c04387.
Zhang, L., Brow, R.K., 2011. A Raman study of iron-phosphate crystalline compounds and glasses. J. Am. Ceram. Soc. 94 (9), 3123–3130. https://doi.org/10.1111/j.1551-2916.2011.04486.x.
Zhu, G.M., Tan, W.J., Gu, T.T., Ji, Y.L., Xu, Q.Y., Yang, J.L., Zhu, M.S., 2025. Mechanism of peroxymonosulfate activation by vanadiferous magnetite-biochar composite catalyst: an investigation into the pathway of singlet oxygen generation. Chem. Eng. J. 514. https://doi.org/10.1016/j.cej.2025.163239.